Parameter Identification of a Copper-Base Alloy Using Digital Image Correlation and Application to a Liquid Rocket Engine Combustion Chamber Wall

By Gordan THIEDE,[1] Jörg RICCIUS,[1] and Stefanie REESE[2]

[1] *Institute of Space Propulsion, DLR, Lampoldshausen, Germany*
[2] *Institute of Applied Mechanics, RWTH Aachen University, Aachen, Germany*

(Received June 21st, 2017)

In recent years the cost aspect of the development, production and operation of liquid rocket engines became more and more important with respect to the competitiveness on the commercial satellite launch market. Therefore, one aspect of the development is focused on novel inexpensive hot gas wall materials for inner liners of rocket combustion chambers that can withstand the extreme operational conditions. The copper-base alloy consisting of copper, chromium and zirconium is such an inexpensive material that has the potential to be used as an inner liner material for future rocket combustion chambers. To predict the damage behavior caused by tensile rupture, a viscoplastic model coupled with ductile isotropic damage, crack-closure effect and thermal ageing is defined and implemented as a user-material routine in the commercial finite element package ANSYS. Uniaxial displacement-controlled tensile tests at temperatures up to 1000 K are performed. In contrary to traditional extensometer based measurements, an optical stereo camera system based on digital image correlation is used to determine the local strain distribution in the necking area of an hourglass-shaped test sample. The material model's parameters are then least squares fitted and applied to a two-dimensional thermomechanical finite element analysis of a half-channel model representing a rocket engine combustion chamber wall with a simplified geometry and a representative heat flux, pressure level and maximum temperature. This paper shows that digital image correlation can be used to capture the local strain distribution in the necking area of highly ductile copper materials at elevated temperatures. Indeed, the numerical analysis with tensile test based material parameters results in an estimated life time of 13 cycles but thinning and bulging of the hot gas wall could not be reproduced.

Key Words: Material parameter identification, Digital image correlation, Continuum damage mechanics, Finite element analysis, Rocket combustion chamber

Nomenclature

α	:	thermal expansion coefficient
$\alpha_i, \beta_i, \gamma_i$	:	thermal ageing material parameters
b_i, Q_i	:	isotropic softening / hardening material parameters
b_{kin}, C	:	kinematic hardening material parameters
$\mathcal{C}_{ijkl}^{(i)}$	:	elasticity tensor
D	:	isotropic damage
ε_{ij}	:	strain tensor
η, m	:	viscosity material parameters
E_i	:	modulus of elasticity
F	:	force
$f_{\mathrm{Mises}}, \bar{f}$	:	von Mises' yield criterion, normalized
γ	:	kinematic hardening material parameter
h	:	crack-closure parameter
k, S	:	isotropic damage material parameters
$\dot{\lambda}$	:	plastic multiplier
ν	:	Poisson's ratio
N_i	:	number of cycle i
p	:	accumulated plastic strain
p_D	:	damage threshold
p_i	:	pressure
ψ	:	Helmholtz free energy
q_i	:	heat flux vector
R	:	drag stress
ρ	:	density
s	:	entropy
$\sigma_{ij}, \tilde{\sigma}_{ij}$	:	stress tensor, effective stress tensor
T_{ij}	:	transformation matrix
t	:	time
θ	:	temperature
u	:	displacement
X_{ij}	:	back stress tensor
Y	:	strain energy release rate density
Z	:	necking factor

The international system (SI) of units is used for all physical quantities: m, kg, K, s, W.

1. Introduction

Combustion chamber liner materials of actively cooled rocket engines are exposed to extreme thermomechanical conditions due to the high temperature gradient and the high pressure difference between the hot gas and the cooling channel wall. With regard to the cost aspect of a rocket engine and its development, the usage of inexpensive hot gas wall materials becomes more and more important. Accurate

numerical models can be used to evaluate and to validate potential material candidates without the need of expensive full-scale tests. However, precise modeling of fracture and the structural behavior of the regarded material is a complex process. Just a few firing cycles already lead to thinning and bulging of the hot gas wall towards the hot gas. This failure mechanism is called "doghouse" effect. Schwarz proposed that ductile rupture is responsible for inducing cracks in the hot gas wall and limiting the combustion chambers life.[1)]

In continuum damage mechanics (CDM), isotropic damage is associated as a scalar variable that is related to the critical strain energy release rate density. Accumulation of damage results in necking and a loss of stiffness during tensile deformation.[2)] Usually, uniaxial material tests are carried out by using an extensometer to measure the elongation along a defined length on the test sample's surface (engineering strain). But for ductile materials, the local strains in the necking area are still larger than the strains measured by an extensometer. We assume that the identification of a numerical model's material parameters with the local strain distribution leads to a better prediction of a rocket combustion chamber's life which is still a difficult problem.

In this paper, we also present an approach of material characterization testing by using optical measuring techniques based on digital image correlation (DIC). The principles of DIC are developed and optimized by Peters and Sutton in the early 1980s.[3,4)] The displacement field on a surface is measured by matching two speckle images acquired from a stereo camera system at different loading stages. Therefore, DIC captures the local strain distribution in the necking area during testing very accurate. We used DIC combined with hourglass-shaped test samples and displacement-controlled tensile tests to characterize the copper-base alloy consisting of copper, chromium and zirconium (CuCrZr) up to 1000 K. This is a novel aspect of the paper because usually high strength steels, aluminum alloys, and composite materials as well pure copper samples up to 373.15 K have been investigated yet.[5)] The rapid oxidation and the high ductility of the copper-base alloys at elevated temperatures need to be addressed.

For determining the material parameters of CuCrZr, a viscoplastic material model including isotropic damage, crack-closure effect and thermal ageing is implemented as a user-defined material in ANSYS.[6)] Based on the work of Wu, Ma and Hild and the assumption of ductile failure, we focused on the identification of the ductile damage parameters taking into account the stiffness variation during tensile loading.[7-9)] In addition, we carried out a monotonic loaded tensile test with a test sample's quarter model to validate the obtained material parameter set with respect to necking and rupture.

Finally, we performed a one-way coupled thermomechanical finite element analysis of a rocket combustion chamber segment with CuCrZr as a potential inner liner material. A half-channel model with simplified geometry is used to compute the hot gas wall's deformation and to predict the rocket chamber's life time on the basis of ductile failure.

2. Digital Image Correlation for Material Testing

2.1. GOM – ARAMIS 5M System

The GOM – ARAMIS 5M system is an optical non-contact measuring system based on DIC. The system performs high-precision measurements of 3D coordinates and evaluates 3D surfaces, 3D motion and deformation. ARAMIS 5M compares digital images at different loading stages which are acquired from two synchronized high-resolution cameras (2448 x 2050 Px). By tracking blocks of randomized speckle marks (316 facets with a size of 50 x 90 Px) on an overlapping grid (with a spacing of 28 x 45 Px), the system measures the 3D surface displacement and computes the strain with subpixel accuracy. For high quality images, the speckle marks need to be unique with a range of contrast and intensity levels. Reflections and shadows should be avoided.[10,11)] In our tests, we used white speckle marks made of Al_2O_3 on the coated surface of the hourglass-shaped test samples that can sustain the high temperatures during testing.

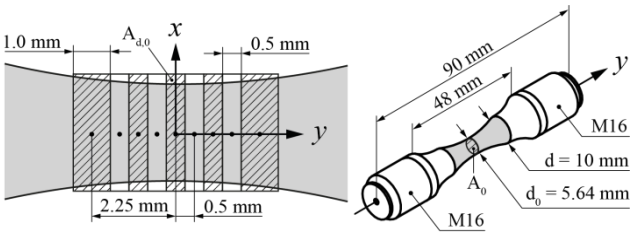

Fig. 1. Test sample with areas for strain averaging and geometry.

Usually, ARAMIS 5M stores the acquired images immediately in the memory of the computer to be correlated after the tests. Due to less memory capacities, this has been done only for the tensile tests. For low-cycle fatigue, stress-relaxation and creep tests, the live function of the ARAMIS 5M system is used. This function enables long-term data acquisition and the results are calculated and recorded instantaneously during the test.[11)] As depicted in Fig. 1, the longitudinal and transversal engineering strains are measured and averaged in narrow rectangular areas in the center of the hourglass-shaped test sample ($A_{d,0}$). The width of the areas is chosen as small as possible. The cross section is assumed to be constant in the center of each area. The axes of the coordinate system are projected onto a hyperbolic pattern to take into account the curved surface.

Another important aspect is that a DIC-based system requires a calibration of the sensors before starting each measurement. A calibration adjusts the position of the cameras with respect to each other. It decreases the intersection error of a 3D point and results in a better accuracy of the correlated strains.[11)] In our tests, we used a square plate as a calibration target with linear strain calculation. The average and maximum intersection error for one representative test was 0.105 Px and 0.700 Px, respectively.

2.2. Test Sample Preparation

According to DIN EN 6072, we used cylindrical hourglass-shaped test samples with a minimal diameter (d_0) of 5.64 mm and M16 threads. This shape allows controlling the necking and the damage localization in the center of the test sample. In addition, the length of the threads is elongated

by 5 mm each due to the clamping mechanism of the servo-hydraulic testing machine. The raw material for the test samples is procured as a cold-worked plate made of CuCrZr. Wire-cut electric discharge machining (EDM) is used to cut out blocks in the longitudinal plane of the plate. Then, each block is drilled to obtain the final test sample's geometry. Note that no test samples could be manufactured out of the plate's thickness direction to investigate anisotropic effects.

Furthermore, a special coating with high absorption is applied on the test sample's surface by means of physical vapor deposition (PVD). This multi-layer coating avoids oxidation of the copper surface at high temperatures. An evolved brittle oxidation layer could lead to cracks of the coating and consequently to inaccurate strain correlation during the optical deformation measurement. Hence, the multi-layer coating on the sample has to be as ductile as possible to ensure the strain measurement until the end of the test.

Taking into account thermal ageing of the structure, a series of test samples is exposed to temperatures at 600 K, 800 K and 1000 K over a period of time 0 h, 10 h and 20 h before testing. This artificial heat treatment allows us to determine the change of the phenomenological stress-strain behavior due to precipitation hardening.[1)]

2.3. Experimental Test Setup

Figure 2 depicts the experimental setup for the material characterization tests using the optical deformation measurement system ARAMIS 5M with two light spots. The two high-resolution cameras are mounted together with 75 mm objectives at separated angles in direction to the sample's center. A calibration is performed before each measurement under test conditions. The ARAMIS 5M system is used to measure the engineering strains on the test sample's surface where necking is expected. The displacement-controlled tensile tests are carried out on a servo-hydraulic testing system (Schenck PC63M with Instron 8800 control unit) with a maximum load of 40 kN. This servo-hydraulic testing machine measures the force with a load cell and the traverse displacement. Note that strain controlled tests should be preferred but they are difficult to realize with direct coupling of ARAMIS 5M to the servo-hydraulic testing machine. Scattering of strain data could lead to instable controlling of the traverse. Unfortunately, application of an extensometer on the sample's surface for controlling the servo-hydraulic testing machine was not possible in our tests with this test setup (insufficient space). In addition, we used induction heating to heat up the test sample to the test temperature. The connectors of the heating device and the connectors of the testing machine are continuously cooled during the tests (blue hoses). The temperature on the test sample's surface is measured with both a high speed pyrometer (Sensortherm Metis HI16) and an infra-red (IR) camera (InfraTec VarioCAM). The pyrometer controlled directly the inductive heating with a spectral range from 1.45 to 1.8 µm and a temperature range from 673.15 K to 1473.15 K (high resolution). The IR camera is used to measure the temperature distribution on the entire surface of the test sample. This

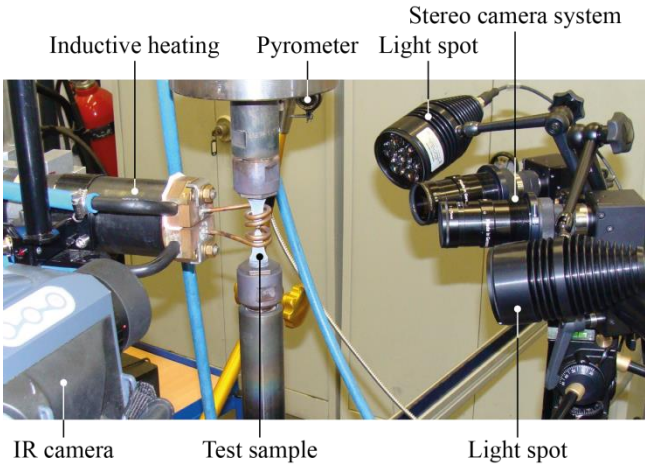

Fig. 2. Experimental test setup with hourglass-shaped test sample.

temperature distribution is used as input for the steady-state thermal finite element analysis. The emissivity coefficient of the pyrometer and the IR camera is set to one. Therefore, a coated dummy sample with a thermocouple mounted in the inside of the sample is used to calibrate the pyrometer and the IR camera together at the three different temperature levels 600 K, 800 K and 1000 K.

Uniaxial quasi-static tensile tests are performed at 600 K, 800 K and 1000 K with a traverse speed of 1 mm/min until rupture. These tensile tests are interrupted to obtain the modulus of elasticity at different loading stages. Then, isotropic damage D can be calculated by

$$D = 1 - \frac{E_i}{E_0}\,, \tag{1}$$

where E_0 and E_i are the moduli of elasticity of the undamaged and damaged material, respectively.[2)] To account for time dependent effects, each reversal point (loading and unloading) is hold for 10 s. Please note that additional tensile tests with an increased traverse speed 5 mm/min and 10 mm/min are carried out with aged test samples as well additional low cycle fatigue tests, stress relaxation tests and creep tests, respectively.

3. Material Modeling and Parameter Identification

3.1. Viscoplastic Damage Model

The material modeling of the viscoplastic model coupled with ductile isotropic damage is based on the work of Tini.[12)] This viscoplastic model is motivated by extending the classical rheological model of Armstrong and Frederick for elastoplastic kinematic hardening.[13)] According to the theory of Lemaitre, ductile isotropic damage is included with respect to the principle of strain equivalence.[2)] Furthermore, crack-closure effect and thermal ageing effects are implemented.[6)] The resulting set of constitutive equations is time discretized with the implicit backward Euler integration scheme.[12)] Implementation of the material model is realized by accessing the finite element program ANSYS with a user-defined material.

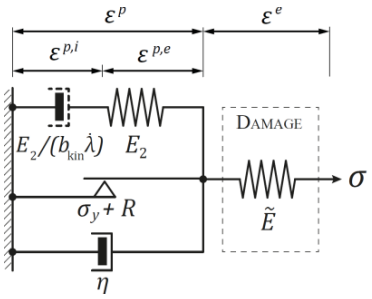

Fig. 3. Rate-dependent rheological model with isotropic damage.

3.1.1. One-Dimensional Rheological Model

In Fig. 3 the extended rheological model for viscoplasticity is depicted basing on the model of Armstrong and Frederick for elastoplastic kinematic hardening.[13] The total mechanical strain ε is decomposed into its elastic ε^e, plastic-elastic $\varepsilon^{p,e}$ and plastic-inelastic $\varepsilon^{p,i}$ parts by

$$\varepsilon = \varepsilon^e + \varepsilon^p = \varepsilon^e + \varepsilon^{p,e} + \varepsilon^{p,i}. \tag{2}$$

The parameters E_2 and $\tilde{E} = E_1(1-D)$ represent the spring stiffness constants for kinematic hardening and for elasticity coupled with isotropic damage, respectively. E_1 is the initial spring constant and $0 \le D \le 1$ is the scalar damage variable. The damage variable influences the elastic behavior of the material.[14] According to Lemaitre,[2] the effective stress $\tilde{\sigma}$ is defined as

$$\tilde{\sigma} = \frac{\sigma}{1-D}. \tag{3}$$

Nonlinear kinematic hardening (with X denoting the back stress) is obtained with E_2 and a rate-independent dashpot $E_2/(b_{\mathrm{kin}}\dot{\lambda})$ where b_{kin} is a material parameter and $\dot{\lambda}$ the plastic multiplier. Using Perzyna formulation,[16] the plastic multiplier in the simplest case is given as

$$\dot{\lambda} = \frac{\langle f_{\mathrm{Mises}} \rangle}{\eta}, \tag{4}$$

where η is a rate-dependent material parameter for viscous effects and $f_{\mathrm{Mises}} = |\sigma - X| - (\sigma_y + R)$ is the von Mises' yield criterion. The von Mises' yield criterion includes the initial yield stress σ_y, the stress due to isotropic hardening (with R denoting the drag stress) and the back stress X.

3.1.2. Continuum Mechanical Approach

On the basis of the extended rheological model and the principle of strain equivalence, the constitutive equations are generalized in three dimensions within the small strain regime. According to the second principle of thermodynamics, the differential form of the Clausius-Duhem inequality can be expressed as

$$\sigma_{ij}\dot{\varepsilon}_{ij} - \rho(\dot{\theta}s + \dot{\psi}) - q_i \frac{\mathrm{grad}\theta}{\theta} \ge 0, \tag{5}$$

where ρ is the density, s is the entropy, ψ is the Helmholtz free energy and q is the heat flux vector. The Helmholtz free energy is a thermodynamic potential that is affected by irreversible processes due to internal structure change of the material.[15] Therefore, the Helmholtz free energy is dependent on the elastic strain ε^e_{ij}, on the temperature θ and on the internal state variables $\psi(\varepsilon^e_{ij}, \varepsilon^{pe}_{ij}, D, p, \theta)$. Time derivative of the Helmholtz free energy leads to

$$\dot{\psi} = \frac{\partial\psi}{\partial\varepsilon^e_{ij}}\dot{\varepsilon}^e_{ij} + \frac{\partial\psi}{\partial D}\dot{D} + \frac{\partial\psi}{\partial\varepsilon^{p,e}_{ij}}\dot{\varepsilon}^{p,e}_{ij} + \frac{\partial\psi}{\partial p}\dot{p} + \frac{\partial\psi}{\partial\theta}\dot{\theta}, \tag{6}$$

with the associated variables

$$\begin{aligned} \sigma_{ij} &= \rho\frac{\partial\psi}{\partial\varepsilon^e_{ij}}, \qquad X^{\mathrm{d}}_{ij} = \rho\frac{\partial\psi}{\partial\varepsilon^{p,e}_{ij}}, \qquad R = \rho\frac{\partial\psi}{\partial p}, \\ \bar{Y} &= -Y = \rho\frac{\partial\psi}{\partial D}, \qquad s = -\frac{\partial\psi}{\partial\theta}. \end{aligned} \tag{7}$$

Inserting the derived Helmholtz free energy Eq. (6) and the additive composition of the total mechanical strain Eq. (2) into the Clausius-Duhem inequality Eq. (5) gives

$$(\sigma_{ij} - X^{\mathrm{d}}_{ij})\dot{\varepsilon}^p_{ij} + X^{\mathrm{d}}_{ij}\dot{\varepsilon}^{p,i}_{ij} - \bar{Y}\dot{D} - R\dot{p} - q_i\frac{\mathrm{grad}\theta}{\theta} \ge 0, \tag{8}$$

with the following constitutive equations of the stress tensors

$$\begin{aligned} \sigma_{ij}(\varepsilon^e_{ij}, D) &= (1-D)\mathcal{C}^{(1)}_{ijkl}\varepsilon^e_{kl}, \\ X^{\mathrm{d}}_{ij}(\varepsilon^{p,e}_{ij}) &= \mathcal{C}^{(2)}_{ijkl}\varepsilon^{p,e}_{kl}, \\ R(p) &= Q_0 p + Q_1(1 - e^{-b_1 p}) + Q_2(1 - e^{-b_2 p}), \\ \bar{Y}(D) &= -\frac{1}{2}\mathcal{C}^{(1)}_{ijkl}\varepsilon^e_{ik}\varepsilon^e_{jl}, \end{aligned} \tag{9}$$

where $Q_{0,1,2}$ and $b_{1,2}$ are material parameters for the drag stress R and $\mathcal{C}^{(1)}_{ijkl}$ and $\mathcal{C}^{(2)}_{ijkl}$ are forth-order elasticity tensors. The evolution equations for the material model are given as follows

$$\begin{aligned} \dot{\varepsilon}^p_{ij} &= \dot{\lambda}\frac{\partial f_{\mathrm{Mises}}}{\partial\sigma_{ij}} = \frac{\dot{\lambda}}{1-D}\frac{\tilde{\sigma}^{\mathrm{d}}_{ij} - X^{\mathrm{d}}_{ij}}{\left\|\tilde{\sigma}^{\mathrm{d}}_{ij} - X^{\mathrm{d}}_{ij}\right\|}, \\ \dot{\varepsilon}^{p,i}_{ij} &= \dot{\lambda}b_{\mathrm{kin}}\dot{\varepsilon}^{p,e\,\mathrm{d}}_{ij}, \\ \dot{p} &= -\dot{\lambda}\frac{\partial f_{\mathrm{Mises}}}{\partial X^{\mathrm{d}}_{ij}} = \sqrt{\tfrac{2}{3}}\dot{\lambda}, \\ \dot{D} &= -\dot{\lambda}\frac{\partial f_{\mathrm{Mises}}}{\partial Y} = \frac{\dot{\lambda}}{1-D}\sqrt{\tfrac{2}{3}}\left(\frac{Y}{S}\right)^k \langle p - p_D \rangle, \end{aligned} \tag{10}$$

with the von Mises' yield criterion f_{Mises} corresponding to J_2 flow theory [2]

$$f_{\mathrm{Mises}} = \left\|\tilde{\sigma}^{\mathrm{d}}_{ij} - X^{\mathrm{d}}_{ij}\right\| - \sqrt{\tfrac{2}{3}}(\sigma_{\mathrm{y}} + R), \tag{11}$$

and the plastic multiplier $\dot{\lambda}$ using Perzyna formulation[16]

$$\dot{\lambda} = \frac{\langle \bar{f}_{\mathrm{Mises}}{}^m \rangle}{\eta}, \tag{12}$$

where m and η are the viscous material parameters, $\|\cdot\|$ defines the tensor norm, $\langle\cdot\rangle$ defines the Macauley brackets and $(\cdot)^{\mathrm{d}}$ denotes the deviatoric part of the tensor. The normalized von Mises' yield criterion is given by

$$\bar{f}_{\mathrm{Mises}} = \frac{\left\|\tilde{\sigma}^{\mathrm{d}}_{ij} - X^{\mathrm{d}}_{ij}\right\|}{\sqrt{\tfrac{2}{3}}(\sigma_{\mathrm{y}} + R)} - 1. \tag{13}$$

Finally, the Kuhn-Trucker relation $\dot{\lambda} \ge 0$, $f_{\mathrm{Mises}} \le 0$, $\dot{\lambda} f_{\mathrm{Mises}} = 0$ has to be satisfied for the constitutive equations of this model.[15]

3.1.3. Extension with Crack-Closure Effect

Within the unified framework of isotropic damage, the modulus of elasticity in tension is assumed to be similar to the modulus of elasticity in compression. But microcracks may open and may close during cyclic loading. According to Lemaitre,[2] this effect influences the modulus of elasticity and the stress state, respectively. For the three-dimensional stress

state it is difficult to determine the loading direction (tension or compression) by means of a scalar quantity. Therefore, the effective stress tensor $\tilde{\sigma}_{ij}$ is first transformed into the principal values $\tilde{\sigma}_{ij}^{\mathrm{diag}}$ and then decomposed into its positive $\langle\tilde{\sigma}_{ij}\rangle$ and negative $\langle-\tilde{\sigma}_{ij}\rangle$ part by

$$\tilde{\sigma}_{ij} = T_{ik}T_{jl}\tilde{\sigma}_{kl}^{\mathrm{diag}}, \tag{14}$$

with

$$\tilde{\sigma}_{ij}^{\mathrm{diag}} = \langle\tilde{\sigma}_{ij}\rangle - \langle-\tilde{\sigma}_{ij}\rangle, \tag{15}$$

where T_{ij} is the orthogonal transformation matrix used for diagonalization. Note that $\langle\tilde{\sigma}_{ij}\rangle$ and $\langle-\tilde{\sigma}_{ij}\rangle$ consist of the eigenvalues of the diagonalized effective stress tensor. Taking into account the crack-closure parameter h in compression, the diagonalized stress tensor $\sigma_{ij}^{\mathrm{diag}}$ is computed by

$$\sigma_{ij}^{\mathrm{diag}} = \langle\tilde{\sigma}_{ij}\rangle(1-D) - \langle-\tilde{\sigma}_{ij}\rangle(1-hD). \tag{16}$$

With retransformation of $\sigma_{ij}^{\mathrm{diag}}$, we obtain the stress tensor depicted in Eq. (9) including the crack-closure effect. The strain energy release rate density is given by

$$Y = \frac{1+\nu}{2E}\left(\frac{\langle\sigma_{ij}\rangle\langle\sigma_{ij}\rangle}{(1-D)^2} + \frac{h\langle-\sigma_{ij}\rangle\langle-\sigma_{ij}\rangle}{(1-hD)^2}\right) - \frac{\nu}{2E}\left(\frac{\langle\sigma_{kk}\rangle^2}{(1-D)^2} + \frac{h\langle-\sigma_{kk}\rangle^2}{(1-hD)^2}\right). \tag{17}$$

where ν is the Poison's ratio for the elastic case.[2,17]

3.1.4. Extension with Thermal Ageing

Due to changes in the microstructure of the copper-base alloy at high temperatures, the phenomenological stress-strain behavior is affected with respect to time.[1] In this model, the yield stress σ_y is decreased over heating time by

$$\sigma_y(\theta, t_{\mathrm{age}}) = \left(\frac{\alpha_{\mathrm{i}}}{\beta_i + t_{\mathrm{age}}}\right) + \gamma_i, \tag{18}$$

where α_i, β_i and γ_i are material parameters for thermal ageing at the temperature level i.

3.2. Identification Procedure

Prior to determining the material parameters of CuCrZr, we first processed the experimental data acquired by DIC (averaged engineering strain in the middle area $A_{d,0}$ of the test sample) and the load cell of servo-hydraulic testing machine (force, F). Engineering stresses $\sigma = F/A_0$ and engineering strains are transformed into their logarithmic (true) values to take into account the decrease of the initial cross-section A_0 during loading. In addition, we also determined the necking factor $Z = (A_0 - A_{\mathrm{R}})/A_0$ to obtain the true rupture strain $\varepsilon_{\mathrm{tr,R}} = 1 - \sqrt{1-Z}$ for each tensile test. This true rupture strain is applied as a displacement loading in the finite element analysis for material parameter fitting. Note that due to the high ductility of CuCrZr at elevated temperatures, a partial loss of the speckle marks on the test sample's surface may result in a loss of strain measurement.

As a next step, we fitted the material parameters of the viscoplastic model coupled with isotropic damage, crack-closure effect and thermal ageing. Table 1 depicts the material model's parameters. The modulus of elasticity E_1 and the yield stress σ_y are obtained directly from experimental true stress-strain data. Transversal ε_{x} and longitudinal ε_y engineering strains are measured and Poisson's ratio is computed $\nu_1 = -\varepsilon_{\mathrm{x}}/\varepsilon_{\mathrm{y}}$ for the elastic case and is assumed to be $\nu_2 = 0.5$ (incompressibility) for the plastic case. As shown in Bouajila,[18] isotropic softening and hardening behavior can be identified by using stress data in dependency of the accumulated plastic strain $p = 2N_i\Delta\varepsilon_p$ where N_i is the number and $\Delta\varepsilon_p$ is the plastic strain range of each cycle. MATLAB with the method of nonlinear least squares including Levenberg-Marquardt algorithm and bisquare weights is used to fit the initial values for isotropic softening and isotropic hardening Q_0, Q_1, Q_2, b_1 and b_2. In addition, the initial temperature dependent thermal ageing parameters α_i, β_i and γ_i are also fitted with MATLAB depending on the decreased yield stress with respect to temperature and ageing time. Note that we could not observe thermal ageing effects at 600 K and therefore are omitted (see Fig. 5).[6] According to Lemaitre,[2] the crack-closure parameter is set to $h = 0.2$.

Table 1. Overview of the material model's parameters

Effect	Material parameters (total: 23)
Elasticity	$E_1,\ \sigma_y,\ \nu_1$
Kinematic Hardening	$E_2,\ b_{\mathrm{kin}},\ \nu_2 = 0.5$
Isotropic Hardening / Softening	$Q_0,\ Q_1,\ Q_2,\ b_1,\ b_2$
Viscosity	$\eta,\ m$
Damage	$S,\ k, p_D,\ h = 0.2$
Thermal Ageing	$\alpha_{800\mathrm{K}},\ \beta_{800K},\ \gamma_{800K},$ $\alpha_{1000\mathrm{K}},\ \beta_{1000K},\ \gamma_{1000K}$

Then, the material parameters for kinematic hardening (E_2 and b_{kin}), viscosity (η and m) and damage (S and k) are fitted by using the method of conjugated gradients in ANSYS. This method minimizes the objective function f_{obj}

$$\min\left(f_{\mathrm{obj}} = \frac{1}{2}\sum_{i=1}^{N}\left(\sigma_{\mathrm{tr,exp}}(\varepsilon,t,T) - \sigma_{\mathrm{tr,fem}}(\varepsilon,t,T)\right)^2\right) \tag{19}$$

which defines as the sum of squares of the difference between the true stress obtained from experimental data $\sigma_{\mathrm{tr,exp}}$ and the true stress computed by the material model $\sigma_{\mathrm{tr,fem}}$ for every time step.

A quasi-static finite element analysis is carried out with an one-element model (dimensions of 1 x 1 x 1 m) to fit the material parameters. To avoid volumetric locking and shear locking, a 3D solid element with quadratic shape function and reduced integration ($\bar{B}$ method) is used. We also used the calculated true rupture strain as the applied total displacement loading because optical strain measurement could not be performed until the end of each test. Figure 4 shows the experimental and numerical fitted results of the tensile tests at 600 K, 800 K and 1000 K. A good coincidence of the tensile tests at 800 K and 1000 K is obtained. Although, the stress deviates at high strains due to insufficient representation of isotropic hardening and kinematic hardening at 600 K. The cut-off depicts the point where damage starts to accumulate. In addition, the numerical computed stress decrease due to thermal ageing for 0 h, 10 h and 20 h is depicted in Fig. 5. As mentioned previously, thermal ageing is omitted for 600 K and linear interpolated between 800 K and 1000 K. Numerical results at 800 K and 1000 K show a good coincidence with experimental data until the damage threshold is reached.

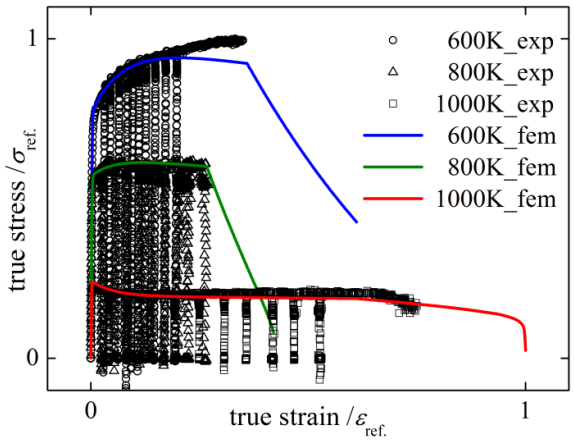

Fig. 4. Experimental and fitted results of the tensile tests in dependency of the temperature.

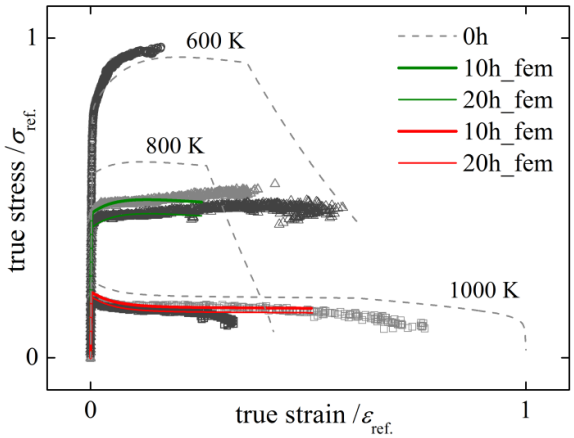

Fig. 5. Experimental and fitted results of the tensile tests in dependency of the temperature and the ageing time.

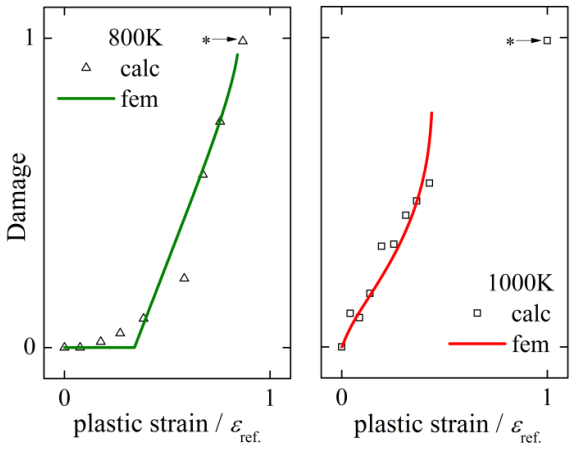

Fig. 6. Damage evolution in dependency of the plastic strain at 800 K and 1000 K. The symbol (*) depicts the calculated rupture strain $\varepsilon_{tr,R} = 1 - \sqrt{1 - Z}$ depending on the necking factor Z.

When damage starts to accumulate, the material softens immediately. Figure 6 shows the experimentally measured damage evolution. The damage threshold p_D is set manually for 800 K and is set to zero for 1000 K. The damage material parameters S and k are fitted to accord with experimental data. As one can see, the calculated rupture strain (*) could not be acquired by the numerical analysis at 1000 K. Note that the modulus of elasticity of the second load step is used as the initial modulus of elasticity (Eq. 1) to calculate damage.

Finally, we performed a structural finite element analysis of a monotonic loaded tensile test with a test sample's quarter model to validate the obtained material parameter set with respect to necking and rupture. The mesh density of the quarter model is set to 24 elements per 5.64 mm. Symmetry boundary conditions are applied at the both centered surfaces. The displacement of the center cross-section A_0 is fixed in length direction. The displacement of the test sample's outer surface is set similar to the displacement of the traverse which is measured by the servo-hydraulic testing machine. Taking into account mesh dependency of this damage model, only the damage parameter S is fitted in a way that damage is nearly 100 % at the measured rupture strain. The damage parameter k remains fixed to ensure a comparable damage gradient. Figure 7 shows the numerical deformation and damage distribution results of the tensile test at 600 K, 800 K and 1000 K. Necking of the monotonic loaded hourglass-shaped test sample at 1000 K is well represented by the model and the used material parameters.

4. Application to a Rocket Chamber Wall Segment

4.1. Finite Element Modeling

The finite element mesh of the rocket combustion chamber segment model is reduced to a slice of a half channel by using rotational symmetry. On the left-hand side of Figure 8, the simplified geometry of the half-channel model is depicted. The entire model consists of 12466 nodes and 2094 elements with quadratic displacement shape functions and reduced integration. Two layers of 3D solid elements are used in thickness direction. A radius of 0.1 mm is applied on the upper cooling channel wall corner to prevent singularity effects.

4.2. Thermal and Structural Analysis

In this work, we performed a one-way coupled thermomechanical 3D analysis of the rocket combustion chamber segment made of the copper-base alloy CuCrZr and nickel. For the thermal analysis, the thermal material parameters of CuCrZr are determined by differential scanning calorimetry (DSC), thermomechanical analysis (TMA) and laser flashing analysis (LMA) measurements. To obtain a maximum temperature of 1000 K on the hot-gas side of the half-channel model, a steady-state thermal analysis of the hot run is carried out with both a heat flux condition of 80 MW/m^2 and convection conditions including a bulk temperature of 74.1 K and a film coefficient of 51000 W/(mm^2 K). Note that the film coefficient is fitted to obtain the maximum temperature on the hot gas side of the cooling channel wall. The computed thermal field is then transferred to a steady-state structural analysis.

The boundary conditions for the structural analysis are set similar to Schwarz.[19] Lateral surfaces of the half-channel model are fixed in φ–direction. The bottom surface is fixed

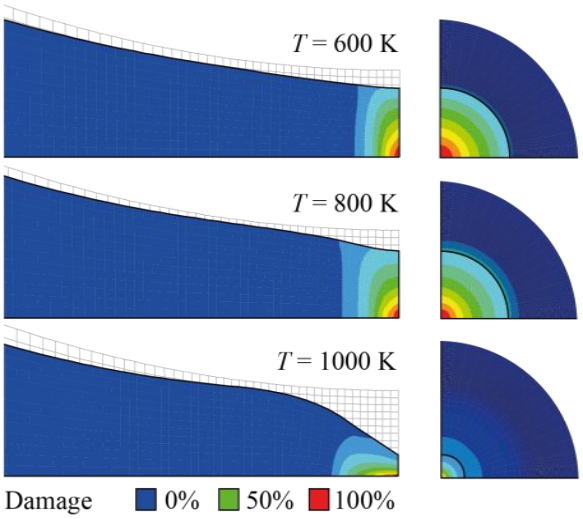

Fig. 7. Comparison of the nodal damage distribution with undeformed edges of the test sample for a monotonic loaded tensile test until rupture in dependency of the temperature.

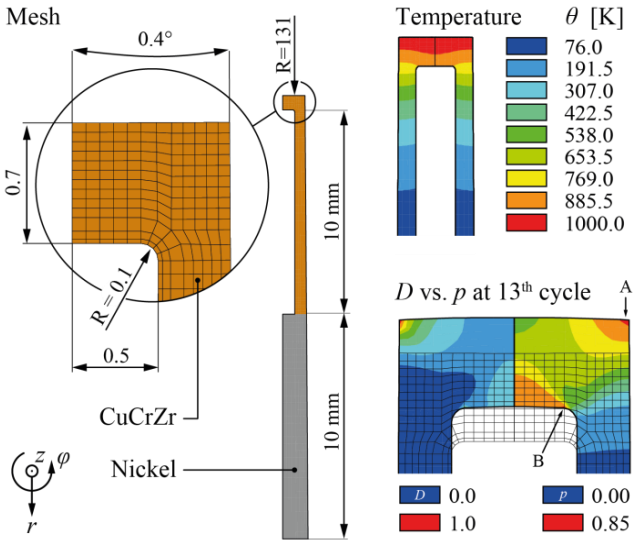

Fig. 8. Mesh with dimensions in mm of the half-channel model, temperature T distribution as input for structural analysis and damage D and accumulated plastic strain p distribution of the 13th cycle.

in z-direction and the upper surface is coupled in z-direction. A hot gas pressure of 200 bar and a cooling channel pressure of 100 bar are applied. Large-deflection effects are included in this structural analysis. The validation cycle is composed into a pre-cooling period of 2 s, a firing period of 600 s, a cooling period of 2 s, and a post-cooling period of 396 s at ambient temperature (total time of one cycle is 1000 s).

4.3. Results

The upper right-hand side of Fig. 8 depicts the temperature distribution as a result of the steady-state thermal analysis. The maximum temperature of 1000 K is located on the hot gas side wall of the half-channel model. This temperature distribution is assumed to be representative for the thermal conditions in a rocket combustion chamber wall during a hot run.

The numerically predicted number of cycles to failure is 13. The predicted damage distribution and the accumulated plastic strain distribution for this rupture cycle are depicted on the lower right-hand side of Fig. 8. The maximum computed damage is located at the upper corner of the cooling channel's fin (see Fig. 8. A). A second damage initiation point is located at corner of the cooling channel (see Fig. 8. B). Indeed, the value of accumulated plastic strain is nearly equal at both damage localization points, but the temperature differs by 200 K. Taking into account the damage evolution at 1000 K with no damage threshold (see Fig. 6), the fitted damage parameters encourage the depicted damage initiation point.

However, a thermally induced tensile deformation with bulging and thinning of the hot gas wall ("doghouse" effect) is not obtained with the depicted cooling channel geometry and the used material parameter set.

5. Conclusion

The objective of this work was to determine the material parameters for the copper-base alloy CuCrZr at high temperatures by the means of DIC and the application to simplified rocket combustion chamber geometry.

Therefore, a test setup with optical deformation measurement system based on DIC is presented. Engineering strains are averaged in static measurement areas with a length of 0.5 mm. Due to high ductility of the copper-base alloy at high temperatures, the necking area could move away from the centered measurement area and could distort the averaged strain measurement. Application of a servo-hydraulic testing machine with two moving traverses would ensure that the necking area is fully covered by the measurement area.

Assuming ductile failure of the combustion chamber wall structure, displacement-controlled interrupted tensile tests up to 1000 K are conducted to identify the material parameters depending on the local strain distribution in the necking area. Because speckle marks tear up at high strains, it is difficult to measure steadily until rupture to obtain the rupture strain in the necking area. This can be addressed by calculating the necking factor depending on the initial and rupture cross section.

In addition, ductile damage parameters are fitted for a viscoplastic material model including isotropic damage, crack-closure effect and thermal ageing in accordance to the measured damage evolution. The fitting is performed by computing only one load step with monotonic tensile loading conditions depending on the calculated rupture strain and time. The reason for this is that scattering of the optical measured strain data leads to an unsteady phenomenological stress-strain behavior and could hardly be used for the material parameter identification procedure.

Finally, the life time and structural degradation of a rocket combustion chamber wall segment is computed. A predicted life time of 13 cycles is obtained and seems to be appropriate. But the damage initiation point is located on the upper corner of the hot gas wall fin and the "doghouse" failure could not be observed with the selected cooling channel geometry and the fitted material parameter set. Taking into account thermomechanical fatigue effects would lead an increased life time and better reproduction of the "doghouse" failure due to increased accumulation of plastic strain.

Acknowledgments

We would like to express our gratitude to Ilja Koch and Andreas Neudecker from the Institute of Lightweight Engineering and Polymer Technology (ILK) of the TU Dresden for realizing and performing the material characterization tests at elevated temperatures by using an optical deformation measurement system based on digital image correlation. We also would like to acknowledge Eva Augenstein from the Fraunhofer Institute for Mechanics of Materials (IWM) for conducting and analyzing the thermophysical characterization tests.

References

1) Schwarz, W., Schwub, S., Quering, K., Wiedmann, D., Höppel H. W. and Göken, M.: Life Prediction of Thermally Highly Loaded Components: Modelling the Damage Process of a Rocket Combustion Chamber Hot Wall, *Council of European Aerospace Societies (CEAS) Space Journal*, **1** (2011), pp. 83-97.
2) Lemaitre, J.: *A Course on Damage Mechanics*, Springer, 1992.
3) Peters, W. H. and Ranson, W. F.: Digital Imaging Techniques In Experimental Stress Analysis, *Optical Engineering*, **21** (1982), pp. 427-431.
4) Sutton, M. A., Wolters, W. J., Peters, W. H., Ranson, W. F. and McNeill, S. R.: Determination of Displacements Using an Improved Digital Correlation Method, *Image and Vision Computing*, **1** (1983), pp. 113-139.
5) Salahouelhadj, A., and Gonzalez, M.: CTE Measurements for 3D Package Substrates Using Digital Image Correlation, 17th International Conference on Thermal, Mechanical and Multi-Physics Simulation and Experiments in Microelectronics and Microsystems, 2016.
6) Thiede, R. G., Riccius, J. R. and Reese, S: Validation of Damage Parameter Based Finite Element Fatigue Life Analysis Results to Combustion Chamber Type TMF Panel Test Results, 52nd AIAA/SAE/ASEE Joint Propulsion Conference, 2016.
7) Wu, T., Coret, M. and Combescure, A.: Strain Localisation and Damage Measurement by Full 3D Digital Image Correlation: Application to 15-5PH Stainless Steel, *Strain*, **47** (2011), pp. 49-61.
8) Ma, N., Takada, K. and Sato, K.: Measurement of Local Strain Path and Identification of Ductile Damage Limit based on Simple Tensile Test, *Procedia Engineering*, **48** (2014), pp. 1402-1407.
9) François, H., Bouterf, A. and Roux, S.: Damage Measurements via DIC, *International Journal of Fracture*, **191** (2015), pp. 77-105.
10) McCormick, N. and Lord, J.: Digital Image Correlation, *Materials today*, **13** (2010), pp. 52-54.
11) GOM mbH: ARAMIS – User Manual – Software (v6.1), 2007
12) Kowollik, D., Tini, V., Reese, S. and Haupt, M.: 3D Fluid–Structure Interaction Analysis of a Typical Liquid Rocket Engine Cycle Based on a Novel Viscoplastic Damage Model, *International Journal for Numerical Methods in Engineering*, **94** (2013), pp. 1165-1190.
13) Frederick, C. O. and Armstrong, P. J.: A Mathematical Representation of the Multiaxial Bauschinger Effect, *Materials at High Temperatures*, **24** (2007), pp. 1-26.
14) Kachanov, L. M.: Rupture Time under Creep Conditions, *International Journal of Fracture*, **97** (1999), pp. 11-18.
15) Murakami, S.: *Continuum Damage Mechanics*, Springer, 2012.
16) Perzyna, P.: Fundamental Problems in Viscoplasticity, *Advances in Applied Mechanics*, **9** (1966), pp. 243-377.
17) Desmorat, R. and Cantournet, S.: Modeling Microdefects Closure Effect with Isotropic/Anisotropic Damage, *International Journal of Damage Mechanics*, **17** (2007), pp. 65-96.
18) Bouajila, W. and Riccius, J. R.: Identication of the Unified Chaboche Constitutive Model's Parameters for a Cost Efficient Copper-Based Alloy, Space Propulsion Conference, 2014.
19) Schwarz, W., Wiedmann, D., Schwub, S., Höppel, H. W. and Göken, M.: Assessment of Different Continuum Damage Models for Life-Time Prediction of High-Thrust Cryogenic Combustion Chambers, 4th European Conference for Aerospace Sciences, 2011.